HHS Public Access

Author manuscript

Cell Rep. Author manuscript; available in PMC 2022 January 03.

Published in final edited form as:

Cell Rep. 2021 November 23; 37(8): 110036. doi:10.1016/j.celrep.2021.110036.

Differentiation of fetal hematopoietic stem cells requires ARID4B to restrict autocrine KITLG/KIT-Src signaling

In-Chi Young[1], **Bogang Wu**[1], **Jaclyn Andricovich**[2,3], **Sung-Ting Chuang**[1], **Rong Li**[1], **Alexandros Tzatsos**[2,3], **Ray-Chang Wu**[1,*], **Mei-Yi Wu**[1,2,4,5,*]

[1]Department of Biochemistry and Molecular Medicine, George Washington University, Washington, DC 20037, USA

[2]Department of Anatomy and Cell Biology, George Washington University, Washington, DC 20037, USA

[3]George Washington University Cancer Center, George Washington University, Washington, DC 20037, USA

[4]Department of Medicine, George Washington University, Washington, DC 20037, USA

[5]Lead contact

SUMMARY

Balance between the hematopoietic stem cell (HSC) duality to either possess self-renewal capacity or differentiate into multipotency progenitors (MPPs) is crucial for maintaining homeostasis of the hematopoietic stem/progenitor cell (HSPC) compartment. To retain the HSC self-renewal activity, KIT, a receptor tyrosine kinase, in HSCs is activated by its cognate ligand KITLG originating from niche cells. Here, we show that AT-rich interaction domain 4B (ARID4B) interferes with KITLG/KIT signaling, consequently allowing HSC differentiation. Conditional *Arid4b* knockout in mouse hematopoietic cells blocks fetal HSC differentiation, preventing hematopoiesis. Mechanistically, ARID4B-deficient HSCs self-express KITLG and overexpress KIT. As to downstream pathways of KITLG/KIT signaling, inhibition of Src family kinases rescues the HSC differentiation defect elicited by ARID4B loss. In summary, the intrinsic ARID4B-KITLG/KIT-Src axis is an HSPC regulatory program that enables the differentiation state, while KIT stimulation by KITLG from niche cells preserves the HSPC undifferentiated pool.

In brief

*Correspondence: rwu@gwu.edu (R.-C.W.), meiyiwu@gwu.edu (M.-Y.W.).

AUTHOR CONTRIBUTIONS

M.-Y.W. and R.-C.W. conceived the study. I.-C.Y., M.-Y.W., and R.-C.W. performed the experiments. I.-C.Y. and B.W. performed flow cytometry and PP2 injection. I.-C.Y. and J.A. performed tail vein injection for competitive transplantation experiments. R.-C.W. and S.-T.C. generated the K562 *ARID4B*KO clones. M.-Y.W. and I.-C.Y. prepared and wrote the manuscript. A.T. provided suggestions with experimental design. M.-Y.W., R.-C.W., and R.L. secured funding.

DECLARATION OF INTERESTS

The authors declare no competing interests.

SUPPLEMENTAL INFORMATION

Supplemental information can be found online at https://doi.org/10.1016/j.celrep.2021.110036.

Hematopoietic stem cells (HSCs) at the top of the hematopoietic hierarchy are able to self-renew and differentiate to mature blood cells. Young et al. report that an HSC self-control mechanism established by ARID4B ensures HSC differentiation. ARID4B-deficient HSCs produce KITLG to stimulate KIT, leading to blockage of HSC differentiation and eventual hematopoietic failure.

Graphical Abstract

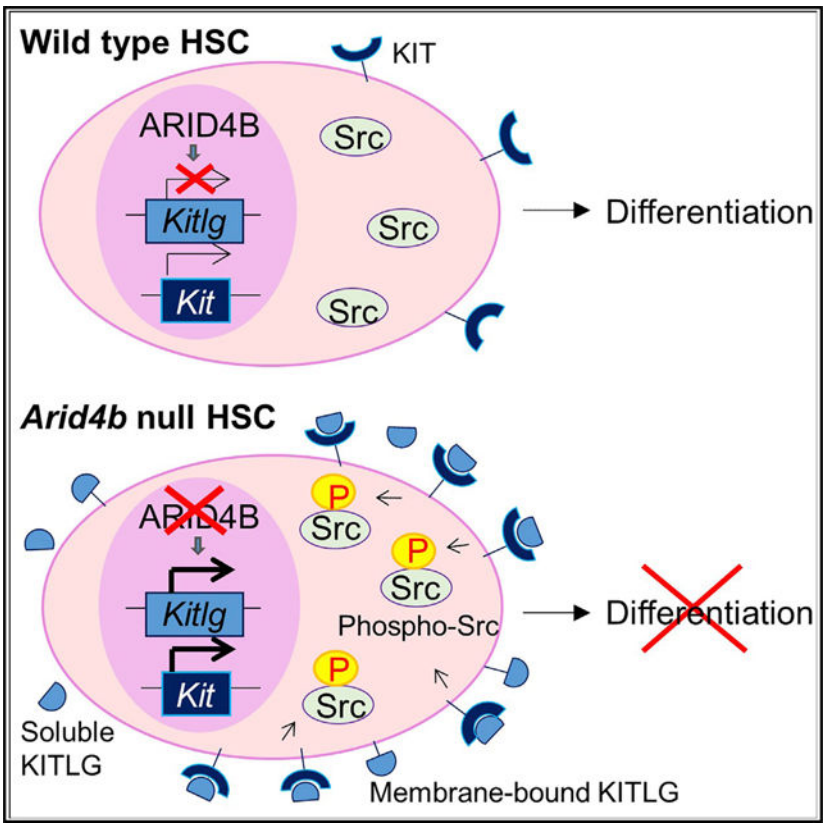

INTRODUCTION

Hematopoietic stem/progenitor cells (HSPCs) reside in a niche in fetal liver (FL) or adult bone marrow (Gao and Liu, 2018; Gao et al., 2018; Khan et al., 2016; Yu and Scadden, 2016), where HSPCs are dependent on interactions with niche cells to serve as a foundational self-renewal reservoir while also giving rise to all blood lineages upon differentiation (Cheng et al., 2020; Laurenti and Göttgens, 2018; Pinho and Frenette, 2019; Wei and Frenette, 2018). The HSPC pool contains hematopoietic stem cells (HSCs) and multipotency progenitors (MPPs). HSCs are heterogeneous in self-renewal capacity, according to the durability of engraftment upon transplantation. Long-term HSCs (LT-HSCs) can produce all hematopoietic cell types in transplantation assays for more than 16 weeks, whereas short-term HSCs (ST-HSCs, also known as MPP1 cells) repopulate transiently in transplants (Laurenti and Göttgens, 2018; Oguro et al., 2013; Yamamoto et al., 2013). HSCs give rise to MPP2 (HPC-2), MPP3 (HPC-1), and MPP4 (HPC-1) cells, which are functionally distinct lineage-biased MPP subsets in adult bone marrow. Among them, no

MPPs can generate other MPPs (Cabezas-Wallscheid et al., 2014; Kiel et al., 2005; Oguro et al., 2013; Pietras et al., 2015; Wilson et al., 2008). Based on its relative myeloid and lymphoid output, MPP2 is a myeloid-biased MPP subset with high megakaryocyte/erythroid (MegE), intermediate granulocyte/macrophage (GM), and low lymphoid potentials. MPP3 is another myeloid-biased MPP subset with high GM, intermediate MegE, and low lymphoid potentials. MPP4 (also known as lymphoid-primed multipotent progenitor [LMPP]) is lymphoid biased and has high lymphoid, intermediate GM, and low MegE potentials (Adolfsson et al., 2005; Oguro et al., 2013; Pietras et al., 2015). These lineage-biased MPPs have no detectable self-renewal ability (Oguro et al., 2013; Pietras et al., 2015).

KIT, a receptor tyrosine kinase expressed in HSCs and hematopoietic progenitor cells (HPCs), becomes downregulated upon differentiation in most lineages (Ogawa et al., 1991, 1993; Okada et al., 1991). *Kit* has been mapped to the murine white spotting (W) locus (Chabot et al., 1988; Geissler et al., 1988). Studies of mice with spontaneous loss-of-function mutations in the W locus highlight the importance of KIT signaling in development of erythrocyte, megakaryocyte, and mast cells (Russell, 1979). In addition, mutations at the W locus in mice are linked to defects in HSC self-renewal activity (Geissler and Russell, 1983; Sharma et al., 2007). On the other hand, mice carrying *Kit* gain-of-function mutation ($Kit^{V558\Delta;\ T669I/+}$) showed enhanced HSC self-renewal (Deshpande et al., 2013).

In bone marrow, KIT ligand KITLG (also known as stem cell factor [SCF]) is expressed in endothelial and leptin receptor-expressing ($LepR^+$) perivascular stromal cells and is a key niche component that maintains HSCs and HPCs. When *Kitlg* was deleted from endothelial cells or $LepR^+$ perivascular stromal cells, HSCs were depleted from bone marrow (Comazzetto et al., 2019; Ding et al., 2012; Xu et al., 2018; Zhou et al., 2017). Adipocytes in bone marrow also secrete KITLG, and deletion of *Kitlg* in adipocytes inhibited hematopoietic regeneration after irradiation (Zhou et al., 2017). In contrast, HSPCs in bone narrow do not express KITLG; therefore, deletion of *Kitlg* from hematopoietic cells did not affect HSPC function (Ding et al., 2012; Zhou et al., 2017). In HSPCs, switching off self-renewal coincides with multilineage priming. Although evidence supports an important role of KITLG/KIT signaling in maintenance of HSC self-renewal capability, whether KITLG/KIT signaling suppresses HSC differentiation to preserve their stem cell state and how *KITLG* and *KIT* are regulated to coordinate HSC self-renewal and differentiation are still unclear.

Epigenetic processes are functionally relevant actions to the genome without altering the underlying DNA sequence. Epigenetic changes most often involve chromatin remodeling that is responsible for reversible modifications on chromatins to control access of genomic DNA to transcription machinery factors and thereby regulate gene expression. AT-rich interaction domain 4B (ARID4B) is a chromatin remodeling protein and belongs to the ARID family (Lin et al., 2014). Proteins of the ARID family have DNA-binding activity with little or no sequence specificity and exhibit diverse functions in development and disease progression (Patsialou et al., 2005; Wilsker et al., 2002). Although ARID4B lacks methyltransferase or acetyltransferase activities, it contains a Tudor domain and a chromo domain. Both Tudor domain and chromo domain mediate protein binding to methylated lysines of histones H3 and H4 (Huang et al., 2006; Lachner et al., 2001; Min et al., 2003;

Sanders et al., 2004) and may function as adaptors to assemble chromatin remodeling complexes (Lu and Wang, 2013; Nishibuchi and Nakayama, 2014). ARID4B has been shown to associate with the HDAC1/Sin3A chromatin remodeling complex (Fleischer et al., 2003).

Previously, we reported that mice with whole-body *Arid4b* deficiency died during early embryogenesis, between embryonic day (E) 3.5 and E7.5 (Wu et al., 2006). ARID4B is required for development of mouse embryonic stem cells into two primary germ layers, mesoderm and endoderm (Terzi Cizmecioglu et al., 2020). In adult mice, haplo-deficiency of *Arid4b* accelerates the onset of acute myeloid leukemia in *Arid4a* null mice, suggesting the role of ARID4B in hematopoietic homeostasis (Wu et al., 2008). In this study, we show that ARID4B inhibits KITLG/KIT signaling to ensure HSCs differentiation.

RESULTS

Mice carrying hematopoietic cell-specific *Arid4b* knockout (KO) die at mid to late gestation

To determine the role of ARID4B in hematopoiesis, we generated a mouse model with conditional *Arid4b* KO in hematopoietic cells (*Arid4b*$^{HC-/-}$, *Arid4b*$^{flox/flox}$; *Vav-iCre*). *Vav-iCre* activity was detected in definitive HSCs at E10.5 onward (Kokavec et al., 2017; Stadtfeld and Graf, 2005). Although all *Arid4b*$^{HC-/-}$ embryos died *in utero* by E18.5 (Figures 1A and 1C), *Arid4b*$^{HC-/-}$ embryos were recovered at E13.5, E14.5, and E16.5 (Figures 1A and 1B). In contrast, their control littermates (*Arid4b*$^{HC+/-}$, *Arid4b*$^{+/flox}$; *Vav-iCre*, and *Arid4b*$^{HC+/+}$, *Arid4b*$^{flox/flox}$) were born in expected numbers (Figures 1A–1C). Morphological examination at E13.5–E16.5 indicated that *Arid4b*$^{HC-/-}$ embryos were pale and anemic, and their FLs, the major hematopoietic organ, were smaller and paler than control littermates (Figure 1B). There was also decreased FL cellularity in *Arid4b*$^{HC-/-}$ embryos (Figure 1E). Histological analysis revealed enlarged cells in *Arid4b*$^{HC-/-}$ FLs at E13.5 and E14.5, but atrophic cells in E16.5 *Arid4b*$^{HC-/-}$ FLs with disrupted structure (Figure 1D), likely resulting from severe anemia causing insufficient tissue oxygenation (Figure 2A).

ARID4B ablation blocks HSC differentiation

Next, we investigated the consequences of ARID4B deficiency in hematopoiesis. Flow cytometry showed severely declined counts of Ter119$^+$ erythroid, Gr-1$^+$ myeloid, and B220$^+$ lymphoid cells in E14.5 *Arid4b*$^{HC-/-}$ FLs (Figures 2A–2C). The numbers of lineage marker-negative (Lin$^-$) cells were reduced in *Arid4b*$^{HC-/-}$ FLs at E13.5 and E14.5 (Figure 2D), and the counts and frequencies of Lin$^-$Sca1$^-$ Kit$^+$ (LS$^-$K) cells that represent the myeloid committed progenitors (Akashi et al., 2000) were also decreased (Figures 2E, S1A, S1B, and S1D). We further analyzed the populations of Lin$^-$Sca1$^+$Kit$^+$ (LSK) cells that encompass the HSPC pool (Morrison et al., 1997; Morrison and Weissman, 1994). Compared with *Arid4b*$^{HC+/+}$ and *Arid4b*$^{HC+/-}$ controls, there was no significant difference in the numbers of LSK cells in *Arid4b*$^{HC-/-}$ FLs at E13.5, but the numbers were decreased at E14.5 (Figure 2F). The percentages of LSK cells in the Lin$^-$ populations were higher in the *Arid4b*$^{HC-/-}$ FLs at both E13.5 and E14.5 (Figures S1A, S1B, and S1E) due to sharply reduced numbers of Lin$^-$ cells (Figure 1D).

We further determined the phenotypic composition of the LSK compartment by flow cytometry. Based on the expression patterns of CD150 and CD48, the LSK compartment can be divided into four HSPC subpopulations, including LT-HSC ($CD150^+CD48^-$LSK), ST-HSC ($CD150^-CD48^-$LSK), MPP2 (HPC-2) ($CD150^+CD48^+$LSK), and MPP3/4 (HPC-1) ($CD150^-CD48^+$LSK) cells (Figure S1A). At the top of the hierarchical hematopoietic system, LT-HSCs give rise to ST-HSCs, and HSCs further differentiate into MPP2, MPP3, and MPP4 cells (Oguro et al., 2013; Pietras et al., 2015; Wilson et al., 2008; Yamamoto et al., 2013). Compared with *Arid4b*$^{HC+/+}$ and *Arid4b*$^{HC+/-}$ controls, similar numbers of LT-HSCs were detected in *Arid4b*$^{HC-/-}$ FLs at E13.5 and E14.5 (Figure 2G), suggesting that ARID4B ablation did not affect LT-HSC self-renewal. The percentages of LT-HSCs in the LSK compartment were higher in E14.5 *Arid4b*$^{HC-/-}$ FLs (Figures S1C and S1F) due to reduced LSK cell numbers (Figure 2F). Notably, the numbers and frequencies of ST-HSCs were significantly increased in E14.5 *Arid4b*$^{HC-/-}$ FLs (Figures 2H, S1C, and S1G), whereas the numbers and frequencies of MPP2 and MPP3/4 cells were decreased (Figures 2I, 2J, S1C, S1H, and S1I). These results suggest that ARID4B ablation blocked HSC differentiation toward MPP2 and MPP3/4 cells and led to accumulation of ST-HSCs. In E16.5 *Arid4b*$^{HC-/-}$ FLs, the numbers of Lin^-, LS^-K, LSK, LT-HSC, ST-HSC, MPP2, and MPP3/4 cells were decreased (Figures S2A–S2G), most likely because of disrupted FL structure (Figure 1D) resulting from severe anemia (Figure 2A).

ARID4B is required for HSPCs to sustain hematopoiesis

To examine the capability of HSPCs at blood cell reconstitution, we isolated KIT^+ cells that contain the HSPC population (Comazzetto et al., 2019) from E13.5 FLs for competitive transplantation assays (Figure 2K). E13.5 FLs were used because the cell numbers of LSK, LT-HSC, ST-HSC, MPP2, and MPP3/4 populations in E13.5 *Arid4b*$^{HC-/-}$ FLs were comparable with E13.5 *Arid4b*$^{HC+/+}$ and *Arid4b*$^{HC+/-}$ controls (Figures 2F–2J). The results showed that KIT^+ cells from E13.5 *Arid4b*$^{HC+/+}$ and *Arid4b*$^{HC+/-}$ FLs (CD45.2) were able to compete with wild-type bone marrow cells from adult mice (CD45.1) to reconstitute blood cells in lethally irradiated recipients (CD45.1) (Figures 2L and 2M). In contrast, the competitiveness of KIT^+ cells from E13.5 *Arid4b*$^{HC-/-}$ FLs (CD45.2) was lost (Figures 2L and 2M), suggesting that ARID4B-deficient HSPCs were unable to sustain hematopoiesis.

ARID4B ablation activates autocrine KITLG/KIT-Src signaling in K562 cells

Given that ablation of ARID4B suppresses early hematopoiesis (Figures 2H–2J) and haplo-deficiency of *Arid4b* advances acute myeloid leukemia in *Arid4a* null mice (Wu et al., 2008), we determined the intrinsic cellular mechanism regulated by ARID4B. Whole-transcriptome analysis (RNA sequencing [RNA-seq]) was performed to compare gene expression profiles of K562 cells with or without KO of *ARID4B* (*ARID4B*KO) (Table S1) (GEO: GSE148273). K562 cells are highly undifferentiated human hematopoietic malignant blasts with multi-potentials that could spontaneously differentiate into progenitors of the erythrocytic, granulocytic, and monocytic series (Lozzio et al., 1981). Functional classification of the differentially expressed genes between K562 control and *ARID4B*KO cells revealed that ARID4B-regulated genes are involved in cell-to-cell signaling and interaction, cellular development, cellular growth and proliferation, hematological diseases, and immunological diseases (Figure S3A). Among these genes, *KITLG* transcripts were

undetectable in K562 control cells but were apparent in K562 *ARID4B*KO cells (Figure S3B). Notably, expression of *KIT*, the KITLG receptor gene, was also increased after *ARID4B* KO (Figure S3B). Independent quantitative reverse transcriptase PCR (qRT-PCR) analysis confirmed that KO of *ARID4B* augmented *KITLG* and *KIT* transcripts (Figure S3C). Furthermore, the protein levels of KITLG and KIT were elevated with ARID4B ablation (Figure S3D); accordingly, the KITLG/KIT downstream effector Src became largely phosphorylated at Tyr416 (Figure S3E), which is required for its activation (Hunter, 1987). The increase of phosphorylated Src was diminished upon treatment with pyrazolopyrimidine 2 (PP2), the Src family kinase inhibitor (Figure S3E). The abundance of phosphorylated Src was also reduced by knockdown of *KIT* using short interfering RNA (siRNA: si*KIT*-1 or si*KIT*-2) (Figure S3F), suggesting that activation of Src is through KIT signaling. These results indicate that ARID4B ablation leads to activation of the KIT-Src axis.

KITLG encodes membrane-bound proteins that can be cleaved by proteases to become soluble (Heissig et al., 2002), and both the membrane-bound and soluble forms of KITLG bind and activate KIT (Martinez-Anton et al., 2019). *KITLG* was expressed in K562 *ARID4B*KO cells, but not control cells (Figure S3B). By introducing conditioned medium that had been pre-incubated with K562 *ARID4B*KO cells for enrichment of soluble KITLG, K562 control cells showed increased Src phosphorylation (Figure S3G). The phosphorylated Src that was elicited by adding conditioned medium declined in K562 control cells with *KIT* knockdown (Figure S3G). These results suggest that soluble KITLG was secreted from K562 *ARID4B*KO cells to conditioned medium and, through KIT activation, induced Src phosphorylation in K562 control cells.

Although RNA-seq analysis identified genes directly or indirectly regulated by ARID4B (Table S1) (GEO: GSE148273), chromatin immunoprecipitation (ChIP) using antibody against ARID4B followed by DNA sequencing (ChIP sequencing [ChIP-seq]) was performed to globally identify direct binding target genes of ARID4B in K562 cells (Table S2) (GEO: GSE148273). Although ChIP-seq analysis showed ARID4B enrichment near the transcriptional start sites of genes (Figures S3H and S3I), ARID4B was not recruited to the promoters of *KIT* or *KITLG* (Table S2) (GEO: GSE148273), which was further confirmed by ChIP-qPCR analysis (Figures S3J and S3K).

Acetylation of lysine 27 on histone H3 (H3K27Ac), an epigenetic mark that is enriched in transcriptional start sites and enhancers, activates promoters by loosening chromatin structure and thereby facilitating assembly of the transcriptional machinery (Pradeepa, 2017). Chromatin remodeling proteins regulate gene expression by modulating epigenetic modifications. Histone deacetylase 1 (HDAC1) is able to deacetylate H3K27Ac and inactivate gene transcription (Li et al., 2016; Tharkar-Promod et al., 2018). ARID4B has been shown to be associated with the HDAC1/Sin3A chromatin remodeling complex and suppress gene transcription in a HDAC1-dependent manner (Fleischer et al., 2003). Interestingly, our ChIP-qPCR analysis showed that ARID4B ablation increased H3K27Ac on the promoters of *KITLG* and *KIT* (Figures S3J and S3K). This result is in agreement with the fact that depletion of ARID4B augmented the *KITLG* and *KIT* transcripts (Figures S3B and S3C), because H3K27Ac is associated with elevated gene transcription (Pradeepa,

2017). In contrast, ARID4B ablation did not affect H3K27Ac on the *MYOD1* promoter (Figures S3J and S3K), indicating that the effects of ARID4B deficiency on the *KITLG* and *KIT* promoters are specific. These results suggest an epigenetic mechanism by which ARID4B ablation activates *KITLG* and *KIT*.

ARID4B restricts autocrine KITLG/KIT signaling in HSPCs

Because KITLG/KIT signaling is critical for HSPC function (Comazzetto et al., 2019; Ding et al., 2012; Geissler and Russell, 1983; Sharma et al., 2007; Xu et al., 2018; Zhou et al., 2017), we determined whether ARID4B regulates expression of KITLG and KIT in HSPCs by flow cytometry. Compared with control FLs, *Arid4b*$^{HC-/-}$ FLs at E14.5 showed that expression of KITLG and KIT was increased in KIT^{+} cells that contain the HSPC population (Figures 3A and 3B). ARID4B was absent in most KIT^{+} cells isolated from E14.5 *Arid4b*$^{HC-/-}$ FLs, which verified successful KO of *Arid4b* (Figure 3C).

However, flow cytometry of living cells revealed the lower levels of surface KIT in KIT^{+} cells of *Arid4b*$^{HC-/-}$ FLs compared with control FLs (Figure S1B). One possible explanation for the lower surface KIT is enhanced receptor-mediated endocytosis that results in increased translocation of KIT from the plasma membrane to the inside of the cells following ligand-induced activation, because *Arid4b*$^{HC-/-}$ FLs expressed a large abundance of KITLG (Figure 3D). We validated KIT internalization by staining both surface and intracellular KIT for flow cytometry using fixed and permeabilized KIT^{+} cells from FLs. The result showed overall increased expression of KIT in *Arid4b*-deficient KIT^{+} cells (Figure 3B). In addition, western blot analysis confirmed the elevated levels of KIT and KITLG in E14.5 *Arid4b*$^{HC-/-}$ FLs, accompanied with markedly increased phosphorylation of their downstream effector Src (Figure 3E), suggesting enhanced KITLG/KIT-Src signaling.

KITLG is produced by niche cells, but not HSPCs (Ding et al., 2012; Zhou et al., 2017). In E14.5 *Arid4b*$^{HC-/-}$ FLs, KIT^{+} cells that contain the HSPC population expressed KITLG (Figure 3A). We further verified KITLG expression in all HSPC populations of E14.5 *Arid4b*$^{HC-/-}$ FLs, including LT-HSCs (Figures 3F and S4A), ST-HSCs (Figures 3G and S4A), MPP2 cells (Figures 3H and S4A), and MPP3/4 cells (Figures 3I and S4A). Quantification analysis showed slightly increased KITLG levels in MPPs compared with HSCs in *Arid4b*$^{HC-/-}$ FLs (Figure 3J). Together, these results demonstrate that ARID4B deficiency in HSPCs induces autocrine KITLG/KIT-Src signaling, in agreement with the results from K562 cells (Figures S3B–S3G).

Inhibiting Src activity completely rescues HSC differentiation to MPPs in *Arid4b*$^{HC-/-}$ FLs

We determined whether the increased KITLG/KIT-Src signaling triggered by loss of ARID4B is responsible for the failure of HSC differentiation in *Arid4b*$^{HC-/-}$ FLs. We treated the *Arid4b*$^{HC-/-}$ embryos with PP2, the Src family kinase inhibitor (Hanke et al., 1996), to interfere with the KITLG/KIT-Src signaling. Pregnant female mice were intravenously injected with PP2 starting from day 10.5 of gestation, because the Cre recombinase driven by the *Vav* promoter was employed to delete the *Arid4b*$^{flox/flox}$ alleles in *Arid4b*$^{HC-/-}$ embryos, and its activity was detected in definitive HSCs at E10.5 onward

(Kokavec et al., 2017; Stadtfeld and Graf, 2005). Although the *Arid4b*$^{HC-/-}$ FLs were pale without treatment of the Src family kinase inhibitor PP2 (Figure 1B), they were pink with PP2 treatment, although still much less red than control FLs (Figure 4A).

Next, we tested the impact of inhibiting KITLG/KIT-Src signaling on hematopoiesis in *Arid4b*$^{HC-/-}$ FLs. After PP2 treatment, the cell numbers and percentages of all HSPC populations, including LT-HSCs, ST-HSCs, MPP2 cells, and MPP3/4 cells, in *Arid4b*$^{HC-/-}$ FLs were comparable with *Arid4b*$^{HC+/+}$ and *Arid4b*$^{HC+/-}$ controls (Figures 4B–4E and S4B–S4E). Accordingly, the counts of LSK cells were similar between *Arid4b*$^{HC-/-}$ and controls FLs (Figure 4F). These results are strikingly different from the E14.5 *Arid4b*$^{HC-/-}$ FLs without PP2 treatment in which differentiation of HSCs was suppressed, as evidenced by increased numbers of ST-HSCs (Figure 2H) and decreased numbers of MPP2 and MPP3/4 cells (Figures 2I and 2J). These data indicate that the blockage of HSC differentiation toward MPPs elicited by ARID4B loss was rescued by PP2, and therefore confirm that ARID4B restricts the KITLG/KIT-Src signaling to ensure HSC differentiation.

On the other hand, inhibition of KITLG/KIT-Src signaling by PP2 did not affect HSC self-renewal in control and *Arid4b*$^{HC-/-}$ mice (Figures S4I and S4J), although KITLG/KIT signaling is critical for self-renewal of HSCs (Comazzetto et al., 2019; Ding et al., 2012; Xu et al., 2018). Therefore, KITLG/KIT signaling might activate other downstream signaling pathways to maintain HSC self-renewal ability. Besides the Src pathway, stimulation of KIT by KITLG could activate the phosphatidylinositol 3-kinase (PI3K), Ras, and JAK2 signaling pathways (Martinez-Anton et al., 2019).

ARID4B is required for development and/or maintenance of myeloid committed progenitors

In spite of the fact that PP2 restores HSC differentiation blocked by loss of ARID4B, *Arid4b*$^{HC-/-}$ FLs still contained lower cellularity than controls even after treatment of PP2 (Figure 4I). The counts of LS^-K and Lin^- cells declined in FLs of the PP2-treated *Arid4b*$^{HC-/-}$ mice (Figures 4G and 4H), which led to higher frequencies of LSK cells but lower percentages of LS^-K and Lin^- cells (Figures S4F–S4H). Consequently, the counts of $Ter119^+$ erythroid, $Gr\text{-}1^+$ myeloid, $B220^+$ lymphoid cells were still decreased in the *Arid4b*$^{HC-/-}$ FLs after PP2 treatment (Figures 4J–4L). These results suggest that ARID4B is also required for development and/or maintenance of lineage-committed progenitor cells, and the involvement of ARID4B extends beyond the KITLG/KIT-Src signaling pathway.

To test differentiation of HSPCs, we performed the colony-forming unit (CFU) assay using FLs of E14.5 *Arid4b*$^{HC+/+}$ and *Arid4b*$^{HC-/-}$ embryos from pregnant female mice that have been intravenously injected with PP2 or vehicle starting from day 10.5 of gestation. CFU assay detected myeloid multipotential progenitors and committed progenitors of the erythroid, monocyte, and granulocyte lineages from *Arid4b*$^{HC+/+}$ FLs, as evidenced by colony formation of mixed CFU-granulocyte/erythrocyte/macrophage/megakaryocyte (CFU-GEMM), CFU-GM, and burst-forming unit-erythroid (BFU-E) (Figures 4M–4O, column 1). In sharp contrast, ARID4B-deficient FL progenitors did not form colony (Figures 4M–4O, column 2). With PP2 treatment, *Arid4b*$^{HC-/-}$ FL progenitors developed CFU-GEMM colonies with the colony numbers comparable with *Arid4b*$^{HC+/+}$ controls

(Figure 4M, columns 3 and 4). This is consistent with the results from flow cytometry analysis that showed MPPs and LSK cells from *Arid4b*$^{HC-/-}$ FLs were restored by PP2 (Figures 4D–4F). These results suggest that inhibition of Src activity by PP2 completely rescued differentiation of HSCs to MPP2, MPP3, and MPP4 subsets, all of which further differentiate toward myeloid multipotential progenitors. MPP2, MPP3, and MPP4 have distinct myeloid potentials, although MPP2 is megakaryocyte biased, MPP3 is myeloid biased, and MPP4 is lymphoid biased (Pietras et al., 2015).

However, PP2 treatment marginally restored CFU-GM and BFU-E colony formation from *Arid4b*$^{HC-/-}$ FL progenitors (Figures 4N and 4O, columns 1–4). This is consistent with the flow cytometry result of PP2-treated *Arid4b*$^{HC-/-}$ FLs showing reduced LS^{-}K population (Figure 4G) that represents the myeloid committed progenitors (Akashi et al., 2000). Using cells from control FLs for the CFU assay, HSCs and MPPs gave rise to CFU-GEMM, CFU-GM, and BFU-E colonies, and downstream myeloid committed progenitors were able to develop CFU-GM and BFU-E colonies (Figures 4M–4O, column 1). Due to deficiency of myeloid committed progenitors in PP2-treated *Arid4b*$^{HC-/-}$ FLs, CFU-GM and BFU-E colonies cannot be completely restored, even though HSCs and MPPs were able to develop small amounts of CFU-GM and BFU-E colonies (Figures 4N and 4O, columns 1–4). Together, besides the blockage of HSC differentiation into MPP2–4 cells, ablation of ARID4B obstructed development and/or proliferation of myeloid committed progenitors.

DISCUSSION

The balance between self-renewal and differentiation of HSPCs is critical for the maintenance of the HSPC compartment (Olson et al., 2020). In this study, we showed that ARID4B is required for differentiation of self-renewable HSCs toward MPPs that have no self-renewal ability (Figure 4P). *Arid4b* KO suppresses differentiation of HSCs into MPP2, MPP3, and MPP4 cells (Figure 4Q). Whereas ARID4B ablation induces a large abundance of the KITLG/KIT-Src signaling, treatment of the Src family kinase inhibitor PP2 rescues the HSC differentiation defect elicited by KO of *Arid4b* (Figure 4R). Together, our data demonstrate that differentiation of HSCs into MPPs requires ARID4B to restrict KITLG/KIT-Src signaling.

Although combinations of surface markers are employed to split the HSPC compartment into functionally distinct subpopulations, including LT-HSC, ST-HSC, MPP2, and MPP3/4 (Cabezas-Wallscheid et al., 2014; Kiel et al., 2005; Oguro et al., 2013; Pietras et al., 2015; Wilson et al., 2008), a recent study on human bone marrow using single-cell RNA-seq (scRNA-seq) proposed a continuum of these low-primed cells, suggesting that the changes between HSCs and MPPs are gradual (Velten et al., 2017). Yet, a question remains as to whether early hematopoiesis is characterized by development of distinct populations or is a continuous process (Laurenti and Göttgens, 2018). A major concern about the continuum-based model is the heavy reliance on scRNA-seq. It is possible that current scRNA-seq methods are not effective to distinguish closely related cell types within the HSPC compartment, because the shared biological processes (e.g., cell cycle and metabolism) generate substantial heterogeneity that overtakes differentially expressed genes between tightly associated stages of early hematopoiesis. Based on protein markers followed by

flow cytometry assays, we were able to demonstrate a slight biological difference between HSCs and MPPs in *Arid4b*$^{HC-/-}$ FL by differential expression of KITLG, suggesting that acquisition of lineage biases in embryonic HSPC cells is not a continuous process. However, there is still a possibility that even though combinations of surface markers easily split the HSPC pool into LT-HSC, ST-HSC, MPP2, and MPP3/4 subpopulations, these functionally distinct cells reside somewhere along a continuous spectrum.

The importance of intercellular communication between HSPCs and the specialized niche microenvironment where niche cells generate growth factors to preserve HSPC function is well recognized (Pinho and Frenette, 2019; Wei and Frenette, 2018). However, HSPC intrinsic regulators that ensure HSPC response to extracellular cues from niche cells remain to be identified. KITLG required for HSC self-renewal is expressed by niche cells and not by HSPCs (Ding et al., 2012; Zhou et al., 2017), and the source of KITLG in the niche microenvironment is a limiting factor for maintenance of HSCs and HPCs (Comazzetto et al., 2019; Ding et al., 2012; Waskow, 2019). Our current findings suggest a self-control mechanism established by ARID4B that restricts HSPCs to self-express *KITLG* and overexpress *KIT*. This HSPC intrinsic regulatory program assures that KITLG signaling could be received only from niche cells, which is another mechanism that limits acquisition of the KITLG/KIT signaling in HSPCs and thereby dictates HSC differentiation.

Limitations of the study

Arid4b KO induced autocrine KITLG/KIT-Src signaling in HSPCs. It will be of interest to directly inhibit *Kit* by applying genetic approaches, such as use of mice with spontaneous loss-of-function mutations in the W locus where *Kit* is located or genetically engineered mice carrying *Kit* deletion in hematopoietic cells. However, *Kit* mutations have been shown to be associated with defects in HSC self-renewal (Geissler and Russell, 1983; Sharma et al., 2007). Therefore, genetic ablation of *Kit* to rescue HSC differentiation in *Arid4b*$^{HC-/-}$ embryos is not achievable. In this study, we used PP2 to interfere with the KITLG/KIT-Src signaling and rescue HSC differentiation in *Arid4b*$^{HC-/-}$ mice without affecting HSC self-renewal.

In vitro targeting *Kit* using siRNA followed by the CFU assay would be another approach to analyze HSC differentiation. Because we use E14.5 *Arid4b*$^{HC+/+}$ and *Arid4b*$^{HC-/-}$ FLs for CFU assay, the embryos still need to be treated *in vivo* with siRNAs to inhibit *Kit* starting from E10.5 to E14.5. This is due to the fact that the Cre recombinase driven by the *Vav* promoter was employed to delete the *Arid4b*$^{flox/flox}$ alleles in hematopoietic cells, and its activity was detected in HSCs at E10.5 onward (Kokavec et al., 2017; Stadtfeld and Graf, 2005). *In vivo* inhibition of *Kit* would suppress HSC self-renewal. In addition, delivery of siRNA to embryos is currently under-developed.

STAR★METHODS

RESOURCE AVAILABILITY

Lead contact—Further information and requests for resources and reagents should be directed to and will be fulfilled by the Lead Contact, Mei-Yi Wu (meiyiwu@gwu.edu).

Materials availability—This study did not generate new unique reagents.

Data and code availability

- RNA-Seq and ChIP-Seq raw data that support our findings of this study were deposited in the Gene Expression Omnibus (https://www.ncbi.nlm.nih.gov/geo/) with the accession code GSE148273.
- This paper does not report original code.
- Any additional information required to reanalyze the data reported in this paper is available from the lead contact upon request.

EXPERIMENTAL MODEL AND SUBJECT DETAILS

Mice—The hematopoietic cell-specific *Arid4b* knockout mice (*Arid4b*$^{HC-/-}$) contain the *Vav*-iCre (the optimized variant of Cre recombinase under the control of the mouse *Vav1* promoter) (de Boer et al., 2003) and the *Arid4b*$^{flox/flox}$ alleles. The *Arid4b*$^{flox/flox}$ mice were previously generated by our laboratory (Wu et al., 2015). The *Vav*-iCre transgenic mice were purchased from The Jackson Laboratory [008610, B6.Cg-Tg(Vav1-icre)A2Kio/J]. The *Arid4b*$^{flox/flox}$ mice and the *Vav*-iCre mice were backcrossed to generate the *Vav*-iCre; *Arid4b*$^{flox/flox}$ (*Arid4b*$^{HC-/-}$), *Vav*-iCre; *Arid4b*$^{+/flox}$ (*Arid4b*$^{HC+/-}$), and *Arid4b*$^{flox/flox}$ (*Arid4b*$^{HC+/+}$) mice. The *Arid4b*$^{HC+/+}$, *Arid4b*$^{HC+/-}$, and *Arid4b*$^{HC-/-}$ mice were analyzed at embryonic day 13.5, 14.5, 16.5, and 18.5 of age and at the neonatal stage. Mice of mixed sex were used for the experiments.

We have complied with all relevant ethical regulations for animal research. Experimental animals and studies were approved by the Institutional Animal Care and User Committee (IACUC) of The George Washington University (protocol number: A208 and A315). All of the mice were bred and maintained at the institution's specific pathogen-free mouse facility. The facility is approved by the American Association for Accreditation of Laboratory Animal Care and operated by current regulations and standards of the US Department of Agriculture and the Department of Health and Human Services.

Cultured cells—Human myelogenous leukemia cell line K562 was purchased from the American Type Culture Collection (ATCC) and were maintained at 37°C in the presence of 5% CO_2. K562 cells were cultured in RPMI 1640 medium (10–040-CV, Corning) supplemented with 10% fetal bovine serum (Atlanta Biologicals).

METHOD DETAILS

Histology and immunohistochemistry—E13.5, E14.5, and E16.5 fetal livers were dissected from the *Arid4b*$^{HC+/+}$ and *Arid4b*$^{HC-/-}$ embryos, and fixed in 4% paraformaldehyde in PBS for 24 hours, processed, and embedded in paraffin. Histological analysis was performed on 5-μm thick paraffin-embedded fetal liver sections by hematoxylin and eosin staining. For immunohistochemistry, antigen retrieval was performed by boiling the paraffin-embedded fetal liver sections in citric acid-based antigen unmasking solution (Vector Laboratories). Samples were blocked with blocking solution (5% donkey serum, 2% bovine serum albumin, and 0.02% Triton X-100 in PBS) and the Mouse on Mouse Blocking

Reagent (Vector Laboratories), followed by incubation with the anti-KITLG (sc-13126, Santa Cruz Biotechnology) antibody in blocking solution. Sections were washed with 0.1% Triton X-100/PBS buffer and incubated with biotinylated donkey anti-mouse secondary antibody (Jackson ImmunoResearch). Signal detection was carried out by the ImmPACT DAB Peroxidase Substrate system (Vector Laboratories). Sections were counterstained with hematoxylin (Sigma-Aldrich). Images were captured with a Nikon Eclipse T*i*-U microscope. Fetal livers of three mice at E13.5 from each genotype of different litters were analyzed.

Isolation of total cells from fetal liver—Pregnant female mice were sacrificed at the chosen day of gestation, and uteri were removed into a tissue culture dish containing PBS. By removing the muscular wall of the uterus, the embryos were transferred to other culture dishes containing PBS to wash away maternal blood contamination. Under a dissection microscope, the fetal liver was isolated by grasping with the fine-tipped forceps. Cells were filtered through a 70-μm strainer (Falcon) to obtain single-cell suspension. Cells were stained with trypan blue, and the cell number was counted using an automated cell counter (Bio-Rad).

For embryos with the treatment of PP2, pregnant female mice were intravenously injected with 2 mg/kg PP2 (S7008, Selleck Chemicals) through tail-vein at the day 10.5 and 12.5 of gestation. The fetal liver of embryos was isolated at E14.5 for flow cytometry analysis and colony-forming unit (CFU) assay.

Isolation of KIT$^+$ cells from fetal liver—KIT$^+$ cells derived from E13.5 or E14.5 fetal livers were collected by magnetic cell sorting with the Anti-APC MultiSort Kit (130–091-255, Miltenyi Biotech). Briefly, single-cell suspensions of fetal liver were blocked with FC Block (553142, 2.4G2, BD Biosciences) in staining buffer (PBS containing 0.2% bovine serum albumin) at 4°C for 5 min, followed by incubation with APC-conjugated anti-KIT antibody (17–1171-83, 2B8, eBioscience) in blocking solution at 4°C for 45 min. After washing with buffer (PBS containing 0.5% bovine serum albumin and 2 mM EDTA), KIT$^+$ cells were magnetically labeled with Anti-APC MultiSort MicroBeads (130–091-255, Miltenyi Biotech) at 4°C for 15 min. The unlabeled cells were removed by passing through the MACS column (130–042-201, Miltenyi Biotech). Finally, magnetic MicroBeads were removed from the KIT positive cells by adding MultiSort Release Reagent (130–091-255, Miltenyi Biotech).

Flow cytometry—For analysis of ARID4B, KIT, and KITLG expression in KIT$^+$ cells, KIT$^+$ cells isolated from E14.5 fetal livers were fixed in 4% paraformaldehyde in PBS for 10 min, then permeabilized with PBS containing 0.2% Triton X-100 for 10 min. For analysis of KIT expression, cells were blocked with FC Block (553142, 2.4G2, BD Biosciences) in staining buffer (PBS containing 0.2% BSA) at 4°C for 5 min, followed by incubation with APC-conjugated anti-KIT antibody (17–1171-83, 2B8, eBioscience) in blocking solution. For analysis of ARID4B and KITLG expression, cells were blocked with blocking solution [5% goat serum (for ARID4B) or 5% donkey serum (for KITLG), 2% bovine serum albumin, and 0.02% Triton X-100 in PBS] at 4°C for 45 min. Cells were incubated with the primary antibodies: anti-ARID4B (A302–233A, Bethyl Laboratories) or anti-KITLG (sc-13126, Santa Cruz Biotechnology) at 4°C for 45 min, followed by incubation with the

appropriate biotin-conjugated secondary antibodies (Jackson ImmunoResearch) at 4°C for 45 min. Cells were then incubated with Alexa Fluor 488 streptavidin (S11223, Invitrogen) at 4°C for 45 min. Signal detection was carried out by flow cytometry analysis.

For analysis of Ter119$^+$ erythroid, Gr-1$^+$ myeloid, B220$^+$ lymphoid cells, single-cell suspensions from E14.5 fetal livers were blocked with FC Block (553142, 2.4G2, BD Biosciences) in staining buffer (PBS containing 0.2% bovine serum albumin) at 4°C for 5 min. Cells were incubated with the biotin-conjugated antibodies against Ter119 (553672, BD Biosciences), Gr-1 (553125, RB6–8C5, BD Biosciences), or B220 (553086, RA3–6B2, BD Biosciences) at 4°C for 45 min in staining buffer. Cells were then incubated with Alexa Fluor 488 streptavidin (S11223, Invitrogen) at 4°C for 45 min. Cells were washed with staining buffer and re-suspended in staining buffer containing DAPI (10236276001, Roche).

For analysis of hematopoietic stem and progenitor cell populations, fetal liver cells were stained with the biotin-conjugated antibody cocktail against the lineage markers [Ter119 (553672, BD Biosciences), Gr-1 (553125, RB6–8C5, BD Biosciences), B220 (553086, RA3–6B2, BD Biosciences), CD4 (553649, H129.19, BD Biosciences), CD5(553019, 53–7.3, BD Biosciences), and CD8a (553029, 53–6.7, BD Biosciences)], together with the LSK-SLAM antibody cocktail containing APC-conjugated anti-KIT (17–1171-83, 2B8, eBioscience), PE-conjugated anti-Sca-1 (553108, D7, BD Biosciences), PE/Cy7-conjugated anti-CD150 (115914, TC15–12F12.2, BioLegend), and APC/Cy7-conjugated anti-CD48 (103432, HM48–1, BioLegend). Cells were then incubated with Alexa Fluor 488-conjugated streptavidin (S11223, Invitrogen). Cells were washed with staining buffer and re-suspended in staining buffer containing DAPI (10236276001, Roche).

For analysis of KITLG expression in LT-HSC, ST-HSC, MPP2, and MPP3/4 cells, fetal liver cells were stained with the biotin-conjugated antibody cocktail against the lineage markers [Ter119 (553672, BD Biosciences), Gr-1 (553125, RB6–8C5, BD Biosciences), B220 (553086, RA3–6B2, BD Biosciences), CD4 (553649, H129.19, BD Biosciences), CD5(553019, 53–7.3, BD Biosciences), and CD8a (553029, 53–6.7, BD Biosciences)], together with the LSK-SLAM antibody cocktail containing FITC-conjugated anti-KITLG (sc-13126 FITC, Santa Cruz Biotechnology), APC-conjugated anti-KIT (17–1171-83, 2B8, eBioscience), PE-conjugated anti-Sca-1 (553108, D7, BD Biosciences), PE/Cy7-conjugated anti-CD150 (115914, TC15–12F12.2, BioLegend), and APC/Cy7-conjugated anti-CD48 (103432, HM48–1, BioLegend). Cells were then incubated with Pacific Blue-conjugated streptavidin (S11222, Invitrogen). Cells were washed with staining buffer and re-suspended in staining buffer containing Viability Ghost Dye 510 (13–0870, Tonbo Bioscience). At least three biological replicates per genotype were analyzed.

Flow cytometry was carried out using BD FACS Celesta (BD Biosciences) and data were analyzed using FlowJo 10.3 software (FlowJo).

Competitive transplantation assay—Adult CD45.1$^+$ recipient mice (B6.SJL-Ptprc^a Pepc^b/BoyJ, 002014, The Jackson Laboratory) were lethally irradiated using a Cesium-137 Gamma irradiator (the Mark I-68A, JL Shepherd and Associates) delivering 9.5 Gy in a single dose. After 4 hours of rest, 3×10^4 KIT$^+$ cells from E13.5 fetal livers of

the donor CD45.2^{+} mice (*Arid4b*$^{HC+/+}$, *Arid4b*$^{HC+/-}$, or *Arid4b*$^{HC-/-}$) mixed with 1 × 10^{6} competitive bone marrow cells from adult CD45.1^{+} mice (B6.SJL-Ptprc^{a} Pepc^{b}/BoyJ, 002014, The Jackson Laboratory) were injected via tail vein into the lethally irradiated CD45.1^{+} recipient mice. One, two, and four months after transplantation, peripheral blood was collected from the orbital sinus of recipient mice and subjected to red blood cell lysis buffer (TNB-4300-L100, TONBO biosciences). Peripheral blood cells were incubated with APC-conjugated anti-CD45.1 (17–0453-81, A20, Invitrogen) and FITC-conjugated anti-CD45.2 (11–0454-81, 104, eBioscience) antibodies, and then were analyzed by flow cytometry (BD FACS Celesta, BD Bioscience).

Colony-Forming Unit (CFU) assay—Colony-forming unit assays using embryos with the treatment of PP2 were performed for detecting myeloid multipotential progenitors and committed progenitors of the erythroid, monocyte, and granulocyte lineages in FLs (Miller and Lai, 2005). Pregnant female mice were intravenously injected with or without 2 mg/kg PP2 (S7008, Selleck Chemicals) through tail-vein at the day 10.5 and 12.5 of gestation. Fetal livers were isolated from embryos at E14.5 age. For CFU assay, total cells from single E14.5 fetal liver of the *Arid4b*$^{HC+/+}$ or *Arid4b*$^{HC-/-}$ embryos were cultured in methylcellulose-based medium (MethoCult™ GF M3434, StemCell Technologies) with or without 10 μM PP2 (S7008, Selleck Chemicals). At least three biological replicates per group were analyzed. Burst-forming unit-erythroid (BFU-E), colony-forming unit-granulocyte/macrophage (CFU-GM), and colony-forming unit granulocyte/erythrocyte/monocyte/macrophage (CFU-GEMM) were tallied at day 13 under the Nikon Eclipse Ti-U microscope.

Western blot analysis—K562 cells were lysed in lysis buffer [20 mM Tris HCl (pH 8.0), 150mM NaCl, 0.5% Nonidet P-40, 2 mM EDTA, protease inhibitor mixture (cOmplete Protease Inhibitor Cocktail, Roche), and phosphatase inhibitor mixture (PhosSTOP, Roche)] for 30 min, followed by centrifugation at 13,400 × g for 20 min at 4°C to clear debris. Fetal livers were lysed in RIPA buffer [25 mM Tris HCl (pH 7.6), 150 mM NaCl, 1% Nonidet P-40, 1% sodium deoxycholate, 0.1% SDS, protease inhibitor mixture (cOmplete Protease Inhibitor Cocktail, Roche), and phosphatase inhibitor mixture (PhosSTOP, Roche)]. For western blot analysis, the samples were resolved by SDS/PAGE and transferred to nitrocellulose membranes (88018, Bio-Rad). After blocking with 5% milk in TBST buffer [20 mM Tris HCl, 150 mM NaCl (pH 7.5), 0.1% Tween 20], the primary antibodies diluted in TBST buffer with 5% milk were added to the membranes for overnight at 4°C, followed by incubation with the appropriate horseradish peroxidase-conjugated secondary antibodies (Jackson ImmunoResearch) for 1 h at room temperature. Signal detection was carried out by Supersignal substrate (Supersignal West Pico Plus Luminol/Enhancer Solution, Thermo Scientific). Subsequent probing with different antibodies was made possible by stripping the membranes with buffer [62.5 mM Tris HCl (pH 6.8), 2% SDS, 100 mM β-mercaptoethanol] at 55°C for 20 min. The primary antibodies used for western blotting were as follows: anti-ARID4B (A302–233A, Bethyl Laboratories), anti-KIT (AF1356, R&D Systems), anti-KITLG (sc-13126, Santa Cruz Biotechnology), anti-Src (2109, 36D10, Cell Signaling Technology), anti-phospho-Src (Y416) (2101, Cell Signaling Technology), and anti-actin (A2228, AC-74, Sigma-Aldrich).

Knockout of ARID4B in K562 cells using CRISPR—To generate the *ARID4B* knockout clone (*ARID4B*KO), K562 cells were transfected with the pLentiCRISPR v2 plasmid that contains *ARID4B* sgRNA (U0898BC010_2, GenScript) using Lipofectamine 2000™ Transfection Reagent (Invitrogen) according to the manufacturers' instructions. Transfected cells were selected by puromycin, and followed by limiting dilution in 96-well plate for monoclonal cell line development. These *ARID4B* sgRNA sequences are AGTTCAGGATGACCACATAA. The level of ARID4B protein in each *ARID4B*KO clone was determined by western blot analysis.

Transfection—Transfection of siRNA into K562 cells was carried out by Lipofectamine RNAiMAX Transfection Reagent (Invitrogen) according to the manufacturers' instructions. Forty-eight hours after transfection, K562 cells were subjected to western blot analysis or differentiation assay. MISSION® Predesigned siRNAs targeting human *KIT* (SASI_Hs01_00088058 and SASI_Hs01_00088060) were purchased from Sigma-Aldrich.

RNA-Seq and qRT-PCR Analysis—Total RNA was purified from wild-type (Control) and *ARID4B*-knockout (*ARID4B*KO) K562 cells using RNeasy Plus Mini kit (74136, QIAGEN) and was treated with DNase I (79254, QIAGEN). Purified RNA was processed for RNA-Seq analysis and initial data analysis (Q^2 Solutions). All data from RNA-Seq analysis were deposited in Gene Expression Omnibus (accession number GSE148273).

For qRT-PCR analysis, two micrograms of DNase I-treated total RNA was used for reverse transcription to synthesize the first-strand cDNA by the Superscript IV First-strand synthesis system (18091200, Invitrogen). qPCR was performed on the ABI StepOne Plus machine (Applied Biosystems) using TaqMan gene expression assays (TaqMan Fast Advanced Master Mix, 4444964, Applied Biosystems). The TaqMan primer/probe sets for genes (4331182, Applied Biosystems) are as follows: *KIT* (Hs00174029_m1), *KITLG* (Hs00241497_m1) and *GAPDH* (Hs03929097_g1). RNA from three samples of each group were analyzed. The levels of gene expression were normalized against the expression level of *GAPDH* in each sample. In each experiment, the normalized level of the gene of interest from one of the control samples was set as 1.

ChIP-Seq analysis—K562 cells were cross-linked using 4% formaldehyde at 37°C for 10 min, and the reaction was quenched by 0.125M glycine for 5 min. Then, cells were processed for ChIP, library preparation, sequencing, and initial data analysis (Active Motif). ChIP assays were performed using the anti-ARID4B antibody (A302–233A, Bethyl Laboratories; dilution 1:100). Input DNA was used for control. Gene calling was based on presence of the ARID4B binding site with 10 kb of the gene margin. All data from ChIP-Seq analysis were deposited in Gene Expression Omnibus (accession number GSE148273).

ChIP-qPCR analysis—ChIP assays were performed as previously described (Wu et al., 2015). K562 cells with or without knockout of ARID4B (*ARID4B*KO and control, respectively) were used for ChIP-qPCR analysis. Chromatin extracted from cells was immunoprecipitated with normal rabbit IgG (P120–101, Bethyl Laboratories), anti-ARID4B (A302–233A, Bethyl Laboratories), or anti-H3K27Ac (ab4729, Abcam) antibodies. DNA from immunoprecipitated chromatin was analyzed by qPCR performed on the ABI StepOne

Plus machine (Applied Biosystems) with Fast SYBR Green Master Mix (4385617, Applied Biosystems).

Bioinformatic analysis—The differentially expressed genes (log_2 |fold change| > 0.59) between K562 *ARID4B*KO and control cells using RNA-Seq analysis were analyzed by Ingenuity Pathway Analysis (IPA, Ingenuity® Systems, QIAGEN IPA). Based on their molecular and cellular functions, these differentially expressed genes were grouped and ranked in the order by significance.

QUANTIFICATION AND STATISTICAL ANALYSIS

All mouse experiments were performed using 3 – 8 mice. All experiments from cell lines were performed using at least three independent experiments in triplicate. All results were shown as the means ± standard errors of the means (SEM). Two-tailed unpaired Student's t test or Wald Chi-square test was used for statistical analysis. *P value*s ≤ 0.05 were considered to be statistically significant. n represents number of mice. Information of the statistical analyses can be found in figures and their associated legends.

Supplementary Material

Refer to Web version on PubMed Central for supplementary material.

ACKNOWLEDGMENTS

This work was supported by the National Cancer Institute (R01CA255996, R01CA188471, R21CA187857, and CA246707) and the McCormick Genomic and Proteomic Center of George Washington University.

REFERENCES

Adolfsson J, Månsson R, Buza-Vidas N, Hultquist A, Liuba K, Jensen CT, Bryder D, Yang L, Borge OJ, Thoren LA, et al. (2005). Identification of Flt3+ lympho-myeloid stem cells lacking erythro-megakaryocytic potential a revised road map for adult blood lineage commitment. Cell 121, 295–306. [PubMed: 15851035]

Akashi K, Traver D, Miyamoto T, and Weissman IL (2000). A clonogenic common myeloid progenitor that gives rise to all myeloid lineages. Nature 404, 193–197. [PubMed: 10724173]

Cabezas-Wallscheid N, Klimmeck D, Hansson J, Lipka DB, Reyes A, Wang Q, Weichenhan D, Lier A, von Paleske L, Renders S, et al. (2014). Identification of regulatory networks in HSCs and their immediate progeny via integrated proteome, transcriptome, and DNA methylome analysis. Cell Stem Cell 15, 507–522. [PubMed: 25158935]

Chabot B, Stephenson DA, Chapman VM, Besmer P, and Bernstein A (1988). The proto-oncogene c-kit encoding a transmembrane tyrosine kinase receptor maps to the mouse W locus. Nature 335, 88–89. [PubMed: 2457811]

Cheng H, Zheng Z, and Cheng T (2020). New paradigms on hematopoietic stem cell differentiation. Protein Cell 11, 34–44. [PubMed: 31201709]

Comazzetto S, Murphy MM, Berto S, Jeffery E, Zhao Z, and Morrison SJ (2019). Restricted Hematopoietic Progenitors and Erythropoiesis Require SCF from Leptin Receptor+ Niche Cells in the Bone Marrow. Cell Stem Cell 24, 477–486.e6. [PubMed: 30661958]

de Boer J, Williams A, Skavdis G, Harker N, Coles M, Tolaini M, Norton T, Williams K, Roderick K, Potocnik AJ, and Kioussis D (2003). Transgenic mice with hematopoietic and lymphoid specific expression of Cre. Eur. J. Immunol. 33, 314–325. [PubMed: 12548562]

Deshpande S, Bosbach B, Yozgat Y, Park CY, Moore MA, and Besmer P (2013). KIT receptor gain-of-function in hematopoiesis enhances stem cell self-renewal and promotes progenitor cell expansion. Stem Cells 31, 1683–1695. [PubMed: 23681919]

Ding L, Saunders TL, Enikolopov G, and Morrison SJ (2012). Endothelial and perivascular cells maintain haematopoietic stem cells. Nature 481, 457–462. [PubMed: 22281595]

Fleischer TC, Yun UJ, and Ayer DE (2003). Identification and characterization of three new components of the mSin3A corepressor complex. Mol. Cell. Biol. 23, 3456–3467. [PubMed: 12724404]

Gao S, and Liu F (2018). Fetal liver: an ideal niche for hematopoietic stem cell expansion. Sci. China Life Sci. 61, 885–892. [PubMed: 29934917]

Gao X, Xu C, Asada N, and Frenette PS (2018). The hematopoietic stem cell niche: from embryo to adult. Development 145, dev139691. [PubMed: 29358215]

Geissler EN, and Russell ES (1983). Analysis of the hematopoietic effects of new dominant spotting (W) mutations of the mouse. II. Effects on mast cell development. Exp. Hematol. 11, 461–466. [PubMed: 6352298]

Geissler EN, Ryan MA, and Housman DE (1988). The dominant-white spotting (W) locus of the mouse encodes the c-kit proto-oncogene. Cell 55, 185–192. [PubMed: 2458842]

Hanke JH, Gardner JP, Dow RL, Changelian PS, Brissette WH, Weringer EJ, Pollok BA, and Connelly PA (1996). Discovery of a novel, potent, and Src family-selective tyrosine kinase inhibitor. Study of Lck- and FynT-dependent T cell activation. J. Biol. Chem. 271, 695–701. [PubMed: 8557675]

Heissig B, Hattori K, Dias S, Friedrich M, Ferris B, Hackett NR, Crystal RG, Besmer P, Lyden D, Moore MA, et al. (2002). Recruitment of stem and progenitor cells from the bone marrow niche requires MMP-9 mediated release of kit-ligand. Cell 109, 625–637. [PubMed: 12062105]

Huang Y, Fang J, Bedford MT, Zhang Y, and Xu RM (2006). Recognition of histone H3 lysine-4 methylation by the double tudor domain of JMJD2A. Science 312, 748–751. [PubMed: 16601153]

Hunter T (1987). A tail of two src's: mutatis mutandis. Cell 49, 1–4. [PubMed: 3030562]

Khan JA, Mendelson A, Kunisaki Y, Birbrair A, Kou Y, Arnal-Estapé A, Pinho S, Ciero P, Nakahara F, Ma'ayan A, et al. (2016). Fetal liver hematopoietic stem cell niches associate with portal vessels. Science 351, 176–180. [PubMed: 26634440]

Kiel MJ, Yilmaz OH, Iwashita T, Yilmaz OH, Terhorst C, and Morrison SJ (2005). SLAM family receptors distinguish hematopoietic stem and progenitor cells and reveal endothelial niches for stem cells. Cell 121, 1109–1121. [PubMed: 15989959]

Kokavec J, Zikmund T, Savvulidi F, Kulvait V, Edelmann W, Skoultchi AI, and Stopka T (2017). The ISWI ATPase Smarca5 (Snf2h) Is Required for Proliferation and Differentiation of Hematopoietic Stem and Progenitor Cells. Stem Cells 35, 1614–1623. [PubMed: 28276606]

Lachner M, O'Carroll D, Rea S, Mechtler K, and Jenuwein T (2001). Methylation of histone H3 lysine 9 creates a binding site for HP1 proteins. Nature 410, 116–120. [PubMed: 11242053]

Laurenti E, and Göttgens B (2018). From haematopoietic stem cells to complex differentiation landscapes. Nature 553, 418–426. [PubMed: 29364285]

Li F, Wu R, Cui X, Zha L, Yu L, Shi H, and Xue B (2016). Histone Deacetylase 1 (HDAC1) Negatively Regulates Thermogenic Program in Brown Adipocytes via Coordinated Regulation of Histone H3 Lysine 27 (H3K27) Deacetylation and Methylation. J. Biol. Chem. 291, 4523–4536. [PubMed: 26733201]

Lin C, Song W, Bi X, Zhao J, Huang Z, Li Z, Zhou J, Cai J, and Zhao H (2014). Recent advances in the ARID family: focusing on roles in human cancer. OncoTargets Ther. 7, 315–324.

Lozzio BB, Lozzio CB, Bamberger EG, and Feliu AS (1981). A multipotential leukemia cell line (K-562) of human origin. Proc. Soc. Exp. Biol. Med. 166, 546–550. [PubMed: 7194480]

Lu R, and Wang GG (2013). Tudor: a versatile family of histone methylation 'readers'. Trends Biochem. Sci. 38, 546–555. [PubMed: 24035451]

Martinez-Anton A, Gras D, Bourdin A, Dubreuil P, and Chanez P (2019). KIT as a therapeutic target for non-oncological diseases. Pharmacol. Ther. 197, 11–37. [PubMed: 30557630]

Miller CL, and Lai B (2005). Human and mouse hematopoietic colony-forming cell assays. Methods Mol. Biol. 290, 71–89. [PubMed: 15361656]

Min J, Zhang Y, and Xu RM (2003). Structural basis for specific binding of Polycomb chromodomain to histone H3 methylated at Lys 27. Genes Dev. 17, 1823–1828. [PubMed: 12897052]

Morrison SJ, and Weissman IL (1994). The long-term repopulating subset of hematopoietic stem cells is deterministic and isolatable by phenotype. Immunity 1, 661–673. [PubMed: 7541305]

Morrison SJ, Wandycz AM, Hemmati HD, Wright DE, and Weissman IL (1997). Identification of a lineage of multipotent hematopoietic progenitors. Development 124, 1929–1939. [PubMed: 9169840]

Nishibuchi G, and Nakayama J (2014). Biochemical and structural properties of heterochromatin protein 1: understanding its role in chromatin assembly. J. Biochem. 156, 11–20. [PubMed: 24825911]

Ogawa M, Matsuzaki Y, Nishikawa S, Hayashi S, Kunisada T, Sudo T, Kina T, Nakauchi H, and Nishikawa S (1991). Expression and function of c-kit in hemopoietic progenitor cells. J. Exp. Med. 174, 63–71. [PubMed: 1711568]

Ogawa M, Nishikawa S, Yoshinaga K, Hayashi S, Kunisada T, Nakao J, Kina T, Sudo T, Kodama H, and Nishikawa S (1993). Expression and function of c-Kit in fetal hemopoietic progenitor cells: transition from the early c-Kit-independent to the late c-Kit-dependent wave of hemopoiesis in the murine embryo. Development 117, 1089–1098. [PubMed: 7686845]

Oguro H, Ding L, and Morrison SJ (2013). SLAM family markers resolve functionally distinct subpopulations of hematopoietic stem cells and multipotent progenitors. Cell Stem Cell 13, 102–116. [PubMed: 23827712]

Okada S, Nakauchi H, Nagayoshi K, Nishikawa S, Nishikawa S, Miura Y, and Suda T (1991). Enrichment and characterization of murine hematopoietic stem cells that express c-kit molecule. Blood 78, 1706–1712. [PubMed: 1717068]

Olson OC, Kang YA, and Passegué E (2020). Normal Hematopoiesis Is a Balancing Act of Self-Renewal and Regeneration. Cold Spring Harb. Perspect. Med. 10, a035519. [PubMed: 31988205]

Patsialou A, Wilsker D, and Moran E (2005). DNA-binding properties of ARID family proteins. Nucleic Acids Res. 33, 66–80. [PubMed: 15640446]

Pietras EM, Reynaud D, Kang YA, Carlin D, Calero-Nieto FJ, Leavitt AD, Stuart JM, Göttgens B, and Passegué E (2015). Functionally Distinct Subsets of Lineage-Biased Multipotent Progenitors Control Blood Production in Normal and Regenerative Conditions. Cell Stem Cell 17, 35–46. [PubMed: 26095048]

Pinho S, and Frenette PS (2019). Haematopoietic stem cell activity and interactions with the niche. Nat. Rev. Mol. Cell Biol. 20, 303–320. [PubMed: 30745579]

Pradeepa MM (2017). Causal role of histone acetylations in enhancer function. Transcription 8, 40–47. [PubMed: 27792455]

Russell ES (1979). Hereditary anemias of the mouse: a review for geneticists. Adv. Genet. 20, 357–459. [PubMed: 390999]

Sanders SL, Portoso M, Mata J, Bähler J, Allshire RC, and Kouzarides T (2004). Methylation of histone H4 lysine 20 controls recruitment of Crb2 to sites of DNA damage. Cell 119, 603–614. [PubMed: 15550243]

Sharma Y, Astle CM, and Harrison DE (2007). Heterozygous kit mutants with little or no apparent anemia exhibit large defects in overall hematopoietic stem cell function. Exp. Hematol. 35, 214–220. [PubMed: 17258070]

Stadtfeld M, and Graf T (2005). Assessing the role of hematopoietic plasticity for endothelial and hepatocyte development by non-invasive lineage tracing. Development 132, 203–213. [PubMed: 15576407]

Terzi Cizmecioglu N, Huang J, Keskin EG, Wang X, Esen I, Chen F, and Orkin SH (2020). ARID4B is critical for mouse embryonic stem cell differentiation towards mesoderm and endoderm, linking epigenetics to pluripotency exit. J. Biol. Chem. 295, 17738–17751. [PubMed: 33454011]

Tharkar-Promod S, Johnson DP, Bennett SE, Dennis EM, Banowsky BG, Jones SS, Shearstone JR, Quayle SN, Min C, Jarpe M, et al. (2018). HDAC1,2 inhibition and doxorubicin impair Mre11-dependent DNA repair and DISC to override BCR-ABL1-driven DSB repair in Philadelphia chromosome-positive B-cell precursor acute lymphoblastic leukemia. Leukemia 32, 49–60. [PubMed: 28579617]

Velten L, Haas SF, Raffel S, Blaszkiewicz S, Islam S, Hennig BP, Hirche C, Lutz C, Buss EC, Nowak D, et al. (2017). Human haematopoietic stem cell lineage commitment is a continuous process. Nat. Cell Biol. 19, 271–281. [PubMed: 28319093]

Waskow C (2019). Spatiotemporal Resolution of SCF Supply in Early Hematopoiesis. Cell Stem Cell 24, 349–350. [PubMed: 30849362]

Wei Q, and Frenette PS (2018). Niches for Hematopoietic Stem Cells and Their Progeny. Immunity 48, 632–648. [PubMed: 29669248]

Wilsker D, Patsialou A, Dallas PB, and Moran E (2002). ARID proteins: a diverse family of DNA binding proteins implicated in the control of cell growth, differentiation, and development. Cell Growth Differ. 13, 95–106. [PubMed: 11959810]

Wilson A, Laurenti E, Oser G, van der Wath RC, Blanco-Bose W, Jaworski M, Offner S, Dunant CF, Eshkind L, Bockamp E, et al. (2008). Hematopoietic stem cells reversibly switch from dormancy to self-renewal during homeostasis and repair. Cell 135, 1118–1129. [PubMed: 19062086]

Wu MY, Tsai TF, and Beaudet AL (2006). Deficiency of Rbbp1/Arid4a and Rbbp1l1/Arid4b alters epigenetic modifications and suppresses an imprinting defect in the PWS/AS domain. Genes Dev. 20, 2859–2870. [PubMed: 17043311]

Wu MY, Eldin KW, and Beaudet AL (2008). Identification of chromatin remodeling genes Arid4a and Arid4b as leukemia suppressor genes. J. Natl. Cancer Inst. 100, 1247–1259. [PubMed: 18728284]

Wu RC, Zeng Y, Pan IW, and Wu MY (2015). Androgen Receptor Coactivator ARID4B Is Required for the Function of Sertoli Cells in Spermatogenesis. Mol. Endocrinol. 29, 1334–1346. [PubMed: 26258622]

Xu C, Gao X, Wei Q, Nakahara F, Zimmerman SE, Mar J, and Frenette PS (2018). Stem cell factor is selectively secreted by arterial endothelial cells in bone marrow. Nat. Commun. 9, 2449. [PubMed: 29934585]

Yamamoto R, Morita Y, Ooehara J, Hamanaka S, Onodera M, Rudolph KL, Ema H, and Nakauchi H (2013). Clonal analysis unveils self-renewing lineage-restricted progenitors generated directly from hematopoietic stem cells. Cell 154, 1112–1126. [PubMed: 23993099]

Yu VW, and Scadden DT (2016). Heterogeneity of the bone marrow niche. Curr. Opin. Hematol. 23, 331–338. [PubMed: 27177311]

Zhou BO, Yu H, Yue R, Zhao Z, Rios JJ, Naveiras O, and Morrison SJ (2017). Bone marrow adipocytes promote the regeneration of stem cells and haematopoiesis by secreting SCF. Nat. Cell Biol. 19, 891–903. [PubMed: 28714970]

Highlights

- HSCs with ARID4B deficiency self-express *KITLG* and overexpress *KIT*
- Autocrine KITLG/KIT signaling phosphorylates Src and blocks HSC differentiation
- Src inhibition rescues the HSC differentiation defect caused by ARID4B ablation

A

Genotype	Expected	E13.5	E14.5	E16.5	Neonatal
Arid4b$^{+/flox}$	25.0%	23.2% (n = 19)	23.6% (n = 43)	22.4% (n = 15)	33.1% (n = 44)
Arid4b$^{flox/flox}$ (*Arid4b*$^{HC+/+}$)	25.0%	28.0% (n = 23)	24.7% (n = 45)	28.4% (n = 19)	34.6% (n = 46)
Arid4b$^{+/flox}$; *Vav-iCre* (*Arid4b*$^{HC+/-}$)	25.0%	25.6% (n = 21)	26.4% (n = 48)	28.4% (n = 19)	32.3% (n = 43)
Arid4b$^{flox/flox}$; *Vav-iCre* (*Arid4b*$^{HC-/-}$)	25.0%	23.2% (n = 19)	25.3% (n = 46)	20.9% (n = 14)	0.0% (n = 0)
Total		82	182	67	133

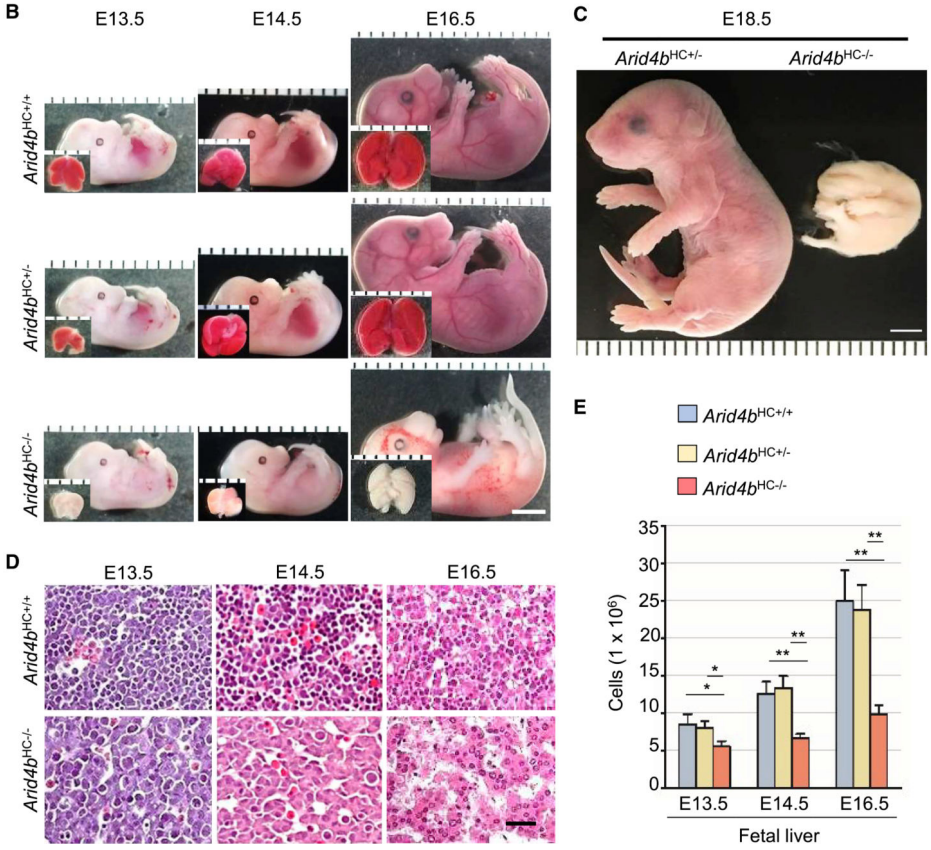

Figure 1. Hematopoietic cell-specific *Arid4b* knockout (*Arid4b*KO) in mice results in anemia and embryonic lethality

(A) Genotype distribution of progenies from the mating of *Arid4b*$^{+/flox}$; *Vav-iCre* female and *Arid4b*$^{flox/flox}$ male mice. Progenies were at E13.5, E14.5, E16.5, or the neonatal stage.

(B) Images of the *Arid4b*$^{HC+/+}$, *Arid4b*$^{HC+/-}$, and *Arid4b*$^{HC-/-}$ embryos and corresponding FLs at E13.5, E14.5, and E16.5. Scale bar, 3 mm.

(C) Images of *Arid4b*$^{HC+/-}$ and *Arid4b*$^{HC-/-}$ embryos at E18.5. Scale bar, 3 mm.

(D) Hematoxylin and eosin staining of FL sections from *Arid4b*$^{HC+/+}$ and *Arid4b*$^{HC-/-}$ embryos at E13.5, E14.5, and E16.5. Scale bar, 20 μm.

(E) Total viable cells in *Arid4b*$^{HC+/+}$, *Arid4b*$^{HC+/-}$, and *Arid4b*$^{HC-/-}$ FLs at E13.5, E14.5, and E16.5. Data are means ± SEM (n ≥ 3). *p < 0.05, **p < 0.01. Statistical analysis: t test.

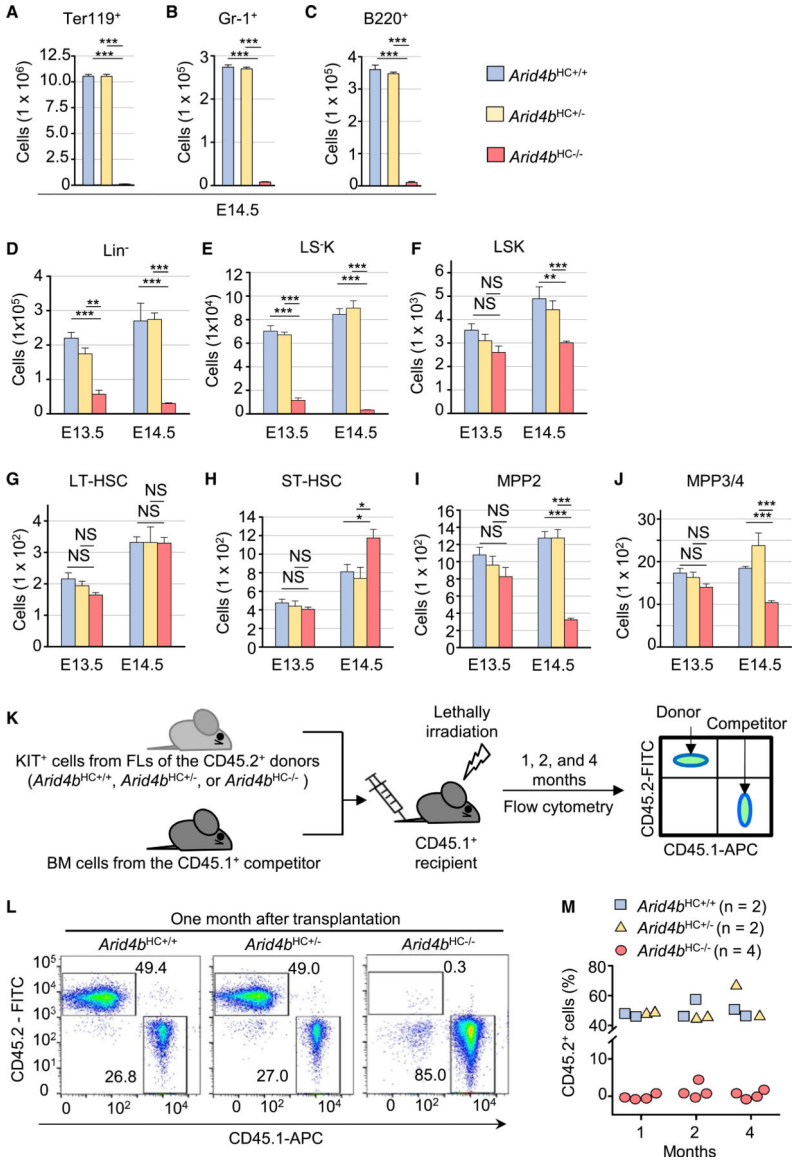

Figure 2. ARID4B ablation blocks HSC differentiation

(A–J) The numbers of Ter119$^+$ erythroid (A), Gr-1$^+$ myeloid (B), B220$^+$ lymphoid (C), Lin$^-$ (D), LS$^-$K (E), LSK (F), LT-HSC (G), ST-HSC (H), MPP2 (I), and MPP3/4 (J) cells in *Arid4b*$^{HC+/+}$, *Arid4b*$^{HC+/-}$, and *Arid4b*$^{HC-/-}$ FLs at E13.5 and/or E14.5. Data are means ± SEM (n ≥ 3). *p < 0.05, **p < 0.01, ***p < 0.001. Statistical analysis: t test.

(K) Scheme of competitive transplantation assay. KIT$^+$ cells from E13.5 *Arid4b*$^{HC+/+}$, *Arid4b*$^{HC+/-}$, or *Arid4b*$^{HC-/-}$ FLs (CD45.2$^+$) mixed with competitive bone marrow (BM) cells from adult wild-type mice (CD45.1$^+$) were injected via tail vein into lethally irradiated recipient mice (CD45.1$^+$). 1, 2, and 4 months after transplantation, CD45.1$^+$ and CD45.2$^+$ cells in peripheral blood cells from the recipient mice were analyzed by flow cytometry.

(L) Flow cytometry plots showing the percentages of CD45.1$^+$ and CD45.2$^+$ cells in peripheral blood of recipient mice (CD45.1$^+$) 1 month after transplantation with KIT$^+$ cells

(CD45.2$^+$) from E13.5 FLs of the indicated genotypes and bone marrow cells (CD45.1$^+$) from wild-type mice.

(M) Percentages of CD45.2$^+$ cells in peripheral blood of recipient mice 1, 2, and 4 months after competitive transplantation.

NS, not significant.

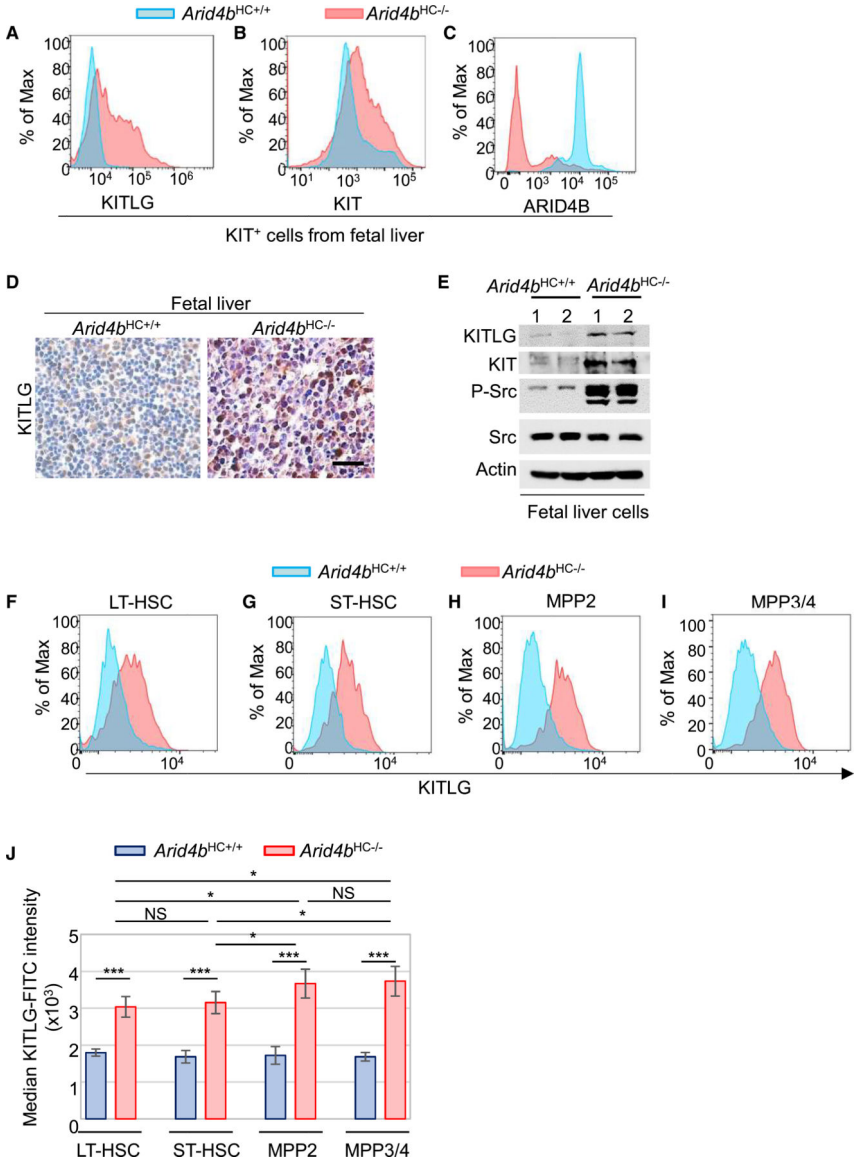

Figure 3. Ablation of ARID4B activates autocrine KITLG/KIT-Src signaling in HSPCs

(A–C) Immunofluorescence staining followed by flow cytometry analyses of KITLG (A), KIT (B), and ARID4B (C) in KIT^{+} cells from E14.5 *Arid4b*$^{HC+/+}$ and *Arid4b*$^{HC-/-}$ FLs.

(D) Immunohistochemistry staining of KITLG in FL sections of E13.5 *Arid4b*$^{HC+/+}$ and *Arid4b*$^{HC-/-}$ embryos. Scale bar, 50 μm.

(E) Western blot analysis showing KITLG, KIT, phospho-Src, and Src in E14.5 *Arid4b*$^{HC+/+}$ and *Arid4b*$^{HC-/-}$ FLs.

(F–J) Immunofluorescence staining followed by flow cytometry analyses of KITLG in LT-HSC (F), ST-HSC (G), MPP2 (H), and MPP3/4 (I) cells from E14.5 *Arid4b*$^{HC+/+}$ and *Arid4b*$^{HC-/-}$ FLs and quantifications (J). Data are means ± SEM (n = 3). *p < 0.05; ***p < 0.001. Statistical analysis: t test.

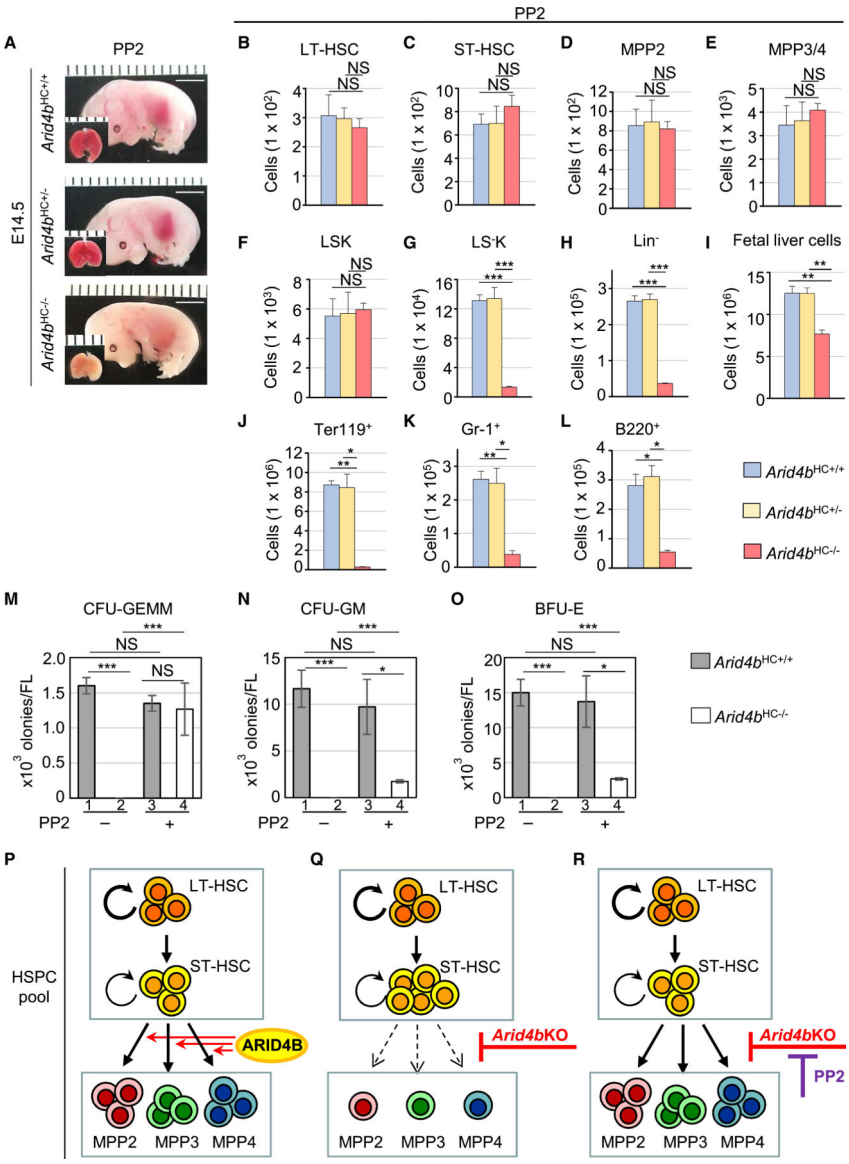

Figure 4. PP2 treatment rescues HSC differentiation in *Arid4b*$^{HC-/-}$ embryos

(A) Images of E14.5 *Arid4b*$^{HC+/+}$, *Arid4b*$^{HC+/-}$, and *Arid4b*$^{HC-/-}$ embryos with PP2 treatment and corresponding FLs. Scale bar, 3 mm.

(B–L) The cell numbers of LT-HSC (B), ST-HSC (C), MPP2 (D), MPP3/4 (E), LSK (F), LS$^-$K (G), Lin$^-$ (H), total viable cells (I), Ter119$^+$ erythroid (J), Gr-1$^+$ myeloid (K), and B220$^+$ lymphoid (L) populations in E14.5 *Arid4b*$^{HC+/+}$, *Arid4b*$^{HC+/-}$, and *Arid4b*$^{HC-/-}$ FLs with PP2 treatment. Data are means ± SEM (n ≥ 3). *p < 0.05, **p < 0.01, ***p < 0.001. Statistical analysis: t test.

(M–O) Quantifications of hematopoietic colony-forming assays using total cells of E14.5 *Arid4b*$^{HC+/+}$ and *Arid4b*$^{HC-/-}$ FLs with or without PP2 for colony formation of CFU-GEMM (M), CFU-GM (N), and BFU-E (O). Data are means ± SEM (n = 3). *p < 0.05, ***p < 0.001. Statistical analysis: t test.

(P–R) Hierarchy of HSCs and MPPs showing that the HSPC pool contains LT-HSCs, ST-HSCs, MPP2 cells, MPP3 cells, and MPP4 cells. Self-renewable LT-HSCs give rise to ST-HSCs that have little self-renewal ability. ARID4B is critical for differentiation of HSCs into MPP2, MPP3, and MPP4 cells (P). *Arid4b*KO suppresses HSC differentiation to MPPs, resulting in ST-HSC accumulation (Q). PP2 treatment rescues the HSC differentiation defect elicited by *Arid4b*KO (R).

KEY RESOURCES TABLE

REAGENT or RESOURCE	SOURCE	IDENTIFIER
Antibodies		
Mouse monoclonal anti-KITLG (G-3)	Santa Cruz Biotechnology	Cat# sc-13126; RRID: AB_628238
Mouse monoclonal anti-KITLG (G-3), FITC-conjugated	Santa Cruz Biotechnology	Cat# sc-13126 FITC; RRID: AB_628238
Rabbit polyclonal anti-ARID4B	Bethyl Laboratories	Cat# A302-233A; RRID: AB_1731051
Rat monoclonal anti-Mouse CD16/CD32 (clone 2.4G2) (Mouse BD Fc Block)	BD Biosciences	Cat# 553142; RRID: AB_394657
Mouse monoclonal anti-CD117 (KIT) (2B8), APC-conjugated	eBioscience	Cat# 17-1171-83; RRID: AB_469431
Rat monoclonal anti-Ter119, biotin-conjugated	BD Biosciences	Cat# 553672; RRID: AB_394985
Rat monoclonal anti-Gr-1 (RB6-8C5), biotin-conjugated	BD Biosciences	Cat# 553125; RRID: AB_394641
Rat monoclonal anti-B220 (RA3-6B2), biotin-conjugated	BD Biosciences	Cat# 553086; RRID: AB_394615
Rat monoclonal anti-CD4 (H129.19), biotin-conjugated	BD Biosciences	Cat# 553649; RRID: AB_394968
Rat monoclonal anti-CD5 (53-7.3), biotin-conjugated	BD Biosciences	Cat# 553019; RRID: AB_394557
Rat monoclonal anti-CD8a (53-6.7), biotin-conjugated	BD Biosciences	Cat# 553029; RRID: AB_394566
Rat monoclonal anti-Sca-1 (D7), PE-conjugated	BD Biosciences	Cat# 553108; RRID: AB_394629
Rat monoclonal anti-CD150 (TC15-12F12.2), PE/Cy7-conjugated	BioLegend	Cat# 115914; RRID: AB_439797
Armenian hamster monoclonal anti-CD48 (HM48-1), APC/Cy7-conjugated	BioLegend	Cat# 103432; RRID: AB_2561463
Mouse monoclonal anti-CD45.1 (A20), APC-conjugated	Invitrogen	Cat# 17-0453-81; RRID: AB_469397
Mouse monoclonal anti- CD45.2 (104), FITC-conjugated	eBioscience	Cat# 11-0454-81; RRID: AB_465060
Goat polyclonal anti-KIT	R&D Systems	Cat# AF1356; RRID: AB_354750
Rabbit monoclonal anti-Src (36D10)	Cell Signaling Technology	Cat# 2109; RRID: AB_2106059
Rabbit polyclonal anti-phospho-Src Y416	Cell Signaling Technology	Cat# 2101; RRID: AB_331697
Mouse monoclonal anti-actin (AC-74)	Sigma-Aldrich	Cat# A2228; RRID: AB_476697
Rabbit polyclonal anti-H3K27Ac	Abcam	Cat# ab4729; RRID: AB_2118291
Donkey polyclonal anti-mouse IgG, biotin-SP-conjugated	Jackson ImmunoResearch Labs	Cat# 715-065-151; RRID: AB_2340785
Donkey polyclonal anti-rabbit IgG, biotin-SP-conjugated	Jackson ImmunoResearch Labs	Cat# 711-066-152; RRID: AB_2340594
Donkey polyclonal anti-mouse IgG, horseradish Peroxidase-conjugated	Jackson ImmunoResearch Labs	Cat# 715-035-151; RRID: AB_2340771
Donkey polyclonal anti-rabbit IgG, horseradish Peroxidase-conjugated	Jackson ImmunoResearch Labs	Cat# 711-035-152; RRID: AB_10015282
Normal donkey serum	Jackson ImmunoResearch Labs	Cat# 017-000-121 RRID: AB_2337258
Normal goat serum	Jackson ImmunoResearch Labs	Cat# 005-000-121 RRID: AB_2336990
Normal rabbit IgG	Bethyl Laboratories	Cat# P120-101; RRID: AB_479829
Chemicals, peptides, and recombinant proteins		
Paraformaldehyde	Electron microscopy sciences	Cat# 19210
Paraffin	Richard-Allan scientific	Cat# 8337
Antigen unmasking solution, citric acid-based	Vector Laboratories	Cat# H-3300-250
Streptavidin, Alexa Fluor 488 conjugate	Invitrogen	Cat# S11223
Streptavidin, Pacific Blue conjugate	Invitrogen	Cat# S11222

REAGENT or RESOURCE	SOURCE	IDENTIFIER
Viability Ghost Dye 510	Tonbo Bioscience	Cat# 13-0870
Bovine serum albumin	RPI Research Products International	Cat# A30075-100.0
Hematoxylin Solution, Mayer's	Sigma-Aldrich	Cat# 51275
70-μm cell strainer	Falcon	Cat# 352350
PP2	Selleck Chemicals	Cat# S7008
DAPI	Roche	Cat# 10236276001
Red blood cell lysis buffer	TONBO biosciences	Cat# TNB-4300-L100
DNase I	QIAGEN	Cat# 79254
Tris	J.T.Baker	Cat# 4099-06
EDTA	BDH	Cat# BDH4142
NaCl	Fisher Scientific	Cat# S271-50
Nonidet P-40	USB	Cat# 19626
Tween 20	BDH	Cat# BDH4210
Triton X-100	Sigma-Aldrich	Cat# T8787
SDS	Fisher Scientific	Cat# BP166-500
β-mercaptoethanol	ACROS	Cat# 125472500
cOmplete (protease inhibitor cocktail tablets)	Roche	Cat# 11697498001
PhosSTOP (phosphatase inhibitor tablets)	Roche	Cat# 4906845001
Nitrocellulose membranes	Bio-Rad	Cat# 88018
RPMI 1640 medium	Corning	Cat# 10-040-CV
Fetal bovine serum	Atlanta Biologicals	Cat# S11150
Formaldehyde	Fisher Scientific	Cat# BP531-500
Glycine	Fisher Scientific	Cat# BP381-5
Critical commercial assays		
M.O.M. (Mouse on Mouse) Blocking Reagent	Vector Laboratories	Cat# MKB-2213-1
ImmPACT DAB Peroxidase Substrate system	Vector Laboratories	Cat# SK-4105
Anti-APC MultiSort Kit (microbeads; release reagent)	Miltenyi Biotech	Cat# 130-091-255
MACS column	Miltenyi Biotech	Cat# 130-042-201
MethoCult™ GF M3434 methylcellulose-based medium	StemCell Technologies	Cat# 03434
RNeasy Plus Mini kit	QIAGEN	Cat# 74136
Superscript IV First-strand synthesis system	Invitrogen	Cat# 18091200
TaqMan Fast Advanced Master Mix	Applied Biosystems	Cat# 4444964
Fast SYBR Green Master Mix	Applied Biosystems	Cat# 4385617
Lipofectamine 2000 Transfection Reagent	Invitrogen	Cat# 11668019
Lipofectamine RNAiMAX Transfection Reagent	Invitrogen	Cat# 13778150
Deposited data		
K562 wild-type and *ARID4BKO* cells RNA-seq dataset	Deposited to Gene Expression Omnibus	GEO accession: SuperSeries GSE148273
*K*562 wild-type cells ARID4B ChIP-seq dataset	Deposited to Gene Expression Omnibus	GEO accession: SuperSeries GSE148273

REAGENT or RESOURCE	SOURCE	IDENTIFIER
Experimental models: Cell lines		
Human: K562 cells	ATCC	Cat# CCL-243
Experimental models: Organisms/strains		
Mouse: B6.Cg-Tg(Vav1-icre)A2Kio/J	Jackson Laboratory	Cat# 008610
Mouse: *Arid4b*$^{flox/flox}$	Wu et al., 2015	N/A
Mouse: B6.SJL-Ptprc^{a} Pepc^{b}/BoyJ, CD45.1^{+}	Jackson Laboratory	Cat# 002014
Oligonucleotides		
TaqMan primer/probe *KIT* (Hs00174029_m1)	Applied Biosystems	Cat# 4331182
TaqMan primer/probe *KITLG* (Hs00241497_m1)	Applied Biosystems	Cat# 4331182
TaqMan primer/probe *GAPDH* (Hs03929097_g1)	Applied Biosystems	Cat# 4331182
ARID4B sgRNA sequences: AGTTCAGGATGACCACATAA	GenScript	Cat# U0898BC010_2
MISSION® Predesigned siRNA (si*KIT*-1)	Sigma-Aldrich	Cat# SASI_Hs01_00088058
MISSION® Predesigned siRNA (si*KIT*-2)	Sigma-Aldrich	Cat# SASI_Hs01_00088060
Primers for ChIP-qPCR analysis: see Table S3	This paper	N/A
Recombinant DNA		
pLentiCRISPR v2 plasmid that contains *ARID4B* sgRNA	GenScript	Cat# U0898BC010_2
Software and algorithms		
FlowJo 10.3	FlowJo	RRID: SCR_008520
Ingenuity Pathway Analysis	QIAGEN	N/A
Other		
Eclipse T*i*-U microscope	Nikon	N/A
Automated cell counter	Bio-Rad	N/A
Cesium-137 gamma irradiator	JL Shepherd and Associates	Mark I-68A
BD FACS Celesta flow cytometer	BD Biosciences	N/A
ABI StepOne Plus	Applied Biosystems	N/A